Nanoscale

ROYAL SOCIETY OF CHEMISTRY

PAPER

View Article Online
View Journal | View Issue

Cite this: *Nanoscale*, 2024, **16**, 15558

Fluorinated polymer zwitterions on gold nanoparticles: patterned catalyst surfaces guide interfacial transport and electrochemical CO_2 reduction†

Qiang Luo, [a] Joseph Tapia, [e] Le Zhou,[d] Chung-Hao Liu, [b,f] Maham Liaqat,[a] Hanyi Duan, [b] Zhefei Yang, [d] Mu-Ping Nieh, [b,c] Todd Emrick, *[d] Peng Bai *[e] and Jie He *[a,b]

We report the use of fluorinated polymer zwitterions to build hybrid systems for efficient CO_2 electroreduction. The unique combination of hydrophilic phosphorylcholine and hydrophobic fluorinated moieties in these polymers creates a fractal structure with mixed branched cylinders on the surface of gold nanoparticles (AuNPs). In the presence of these polymers, the CO faradaic efficiency improves by 50–80% in the range of −0.7 V to −0.9 V. The fractal structures have a domain size of ~3 nm, showing enhanced mass transfer kinetics of CO_2 approaching the catalyst surfaces without limiting ion diffusion. The phase-separated hydrophilic and hydrophobic domains offer separated channeling to water and CO_2, as confirmed by attenuated total reflectance surface-enhanced infrared absorption spectroscopy (ATR-SEIRAS) and molecule dynamic (MD) simulations. H_2O molecules permeate extensively into the polymer layer that adsorbs on zwitterions, forming continuous chains, while CO_2 molecules strongly associate with the fluorinated tails of fluorinated polyzwitterions, with oxygen facing the positively charged amine groups. Overall, this coupling of zwitterion and fluorocarbon in a polymer material creates new opportunities for defining microenvironments of metallic nanocatalysts in hybrid structures.

Received 4th April 2024,
Accepted 28th July 2024

DOI: 10.1039/d4nr01484g

rsc.li/nanoscale

Introduction

The sustainable conversion of CO_2 into valuable chemicals and fuels has attracted considerable attention as a means to reduce CO_2 emission.[1–4] Electroreduction of CO_2 in an aqueous electrolyte stands out as a potential solution to achieve CO_2 cycling in the form of C_1 and C_2 fuels, making use of electricity generated from renewable sources.[5–8] CO_2 electroreduction, however, relies on water as a proton source to drive this chemical transformation.[9] The catalyst-electrolyte-reactant (solid–liquid) interface is strongly hydrated during electrolysis.[10,11] At this interface, an undesirable competitive proton reduction, known as the hydrogen evolution reaction (HER), occurs at a similar thermodynamic potential.[12] Hydrogen production during electroreduction of CO_2 therefore lowers the selectivity or faradaic efficiency (FE), the efficiency associated with utilizing electricity to carry out CO_2 transformation.[13] Happening at the interface of nanocatalysts, the electroreduction of CO_2 is a complex process that is affected by various microenvironmental characteristics. These variables may greatly impact the efficiency, selectivity, and overall performance of the process.[14] One straightforward solution is to control the localized proton/CO_2 concentrations at the solid–liquid interface.[10,11,15] A higher localized pH, *e.g.*, in gas-flow cells or porous catalysts, can lower the proton concentrations while at the same time, it can promote the selectivity for CO_2 electroreduction.[16–23] Notably, mesoporous Au nanostructures with an inverse opal structure could increase the selectivity for CO_2 electroreduction by suppressing HER through diffusional limitations of protons imposed by a porous electrode.[24] Alternatively, by tuning the cation species in electrolytes, the

[a]*Department of Chemistry, University of Connecticut, Storrs, CT 06269, USA. E-mail: jie.he@uconn.edu*
[b]*Polymer Program, Institute of Materials Science, University of Connecticut, Storrs, CT 06269, USA*
[c]*Department of Chemical and Biomolecular Engineering, University of Connecticut, Storrs, CT 06269, USA*
[d]*Polymer Science and Engineering Department, Conte Center for Polymer Research University of Massachusetts, Amherst, Massachusetts 01003, USA. E-mail: tsemrick@mail.pse.umass.edu*
[e]*Department of Chemical Engineering, University of Massachusetts, Amherst, Massachusetts 01003, USA. E-mail: pengbai@umass.edu*
[f]*Neutron Scattering Division, Oak Ridge National Laboratory, Oak Ridge, Tennessee 37831, USA*

† Electronic supplementary information (ESI) available. See DOI: https://doi.org/10.1039/d4nr01484g

strong diploe field created by the hydrated metal cations near the electrode can dramatically lower the adsorption energy of $*CO_2$ and *CO.[25] For example, Cs^+ ions increase the activity of Ag electrodes by 2.4 times, from 59.1% to 80.3%, relative to Li^+ ions.[26]

Modifying nanoparticle catalysts with surface ligands represents an attainable solution to addressing this unmet challenge at the solid–liquid interface.[17,27–32] The key feature of surface-bound ligands is to create a microenvironment that contributes surface gating, *i.e.*, mass transporting of reactants and products.[11,33–35] Such ligands are well-known to control surface hydrophobicity of nanocatalysts.[36–39] By adding hydrophobic surface ligands, surface hydrophobicity has been demonstrated to change the product selectivity on Au,[33,34,40] Ag[41,42] and Cu.[11,43,44] On Cu dendrites, hydrophobic 1-octadecanethiol (ODT) dramatically changed the metal surface from hydrophilic to superhydrophobic with a water contact angle of 153°.[11] Consequently, the hydrophobic pocket captured gaseous CO_2 and favored its reduction with a selectivity ~90% for CO_2 reduction while suppressing HER reaction below 10% at −1.6 V *vs.* reversible hydrogen electrode (RHE, the same hereafter).[11] Unfortunately, this hydrophobicity also lowers the overall activity of Cu because of limited surface wetting (ion diffusion) by the electrolyte. Alternatively, ligands that balance surface hydrophobicity and hydrophilicity create a more dynamic interface without limiting molecular diffusion, with additionally balanced accessibility of CO_2 and water, being key for harmonizing catalyst reactivity without compromising activity.[18,45]

Here we describe a method to control the microenvironment of nanoscale catalysts using polymer zwitterions that balance mass transport of CO_2 and protons under CO_2 electroreduction in an aqueous electrolyte (Scheme 1). The extreme hydrophilicity of zwitterions, such as poly(2-methacryloyloxyethyl phosphoryl choline) (polyMPC, P1), with inner-salt phosphorylcholine (PC) side chains are offset by the integration of fluorocarbon groups into choline phosphate-based polymers P2 and P3.[46] Using these fluorozwitterion copolymers, the CO FE on gold nanoparticles (AuNPs, ~3 nm) improved from ~50% to 80%, with perfluorinated P3 in the range of −0.7 V to −0.9 V, while the partial current density for HER was suppressed by ~50%. The phase-separated hydrophilic zwitterion domains and hydrophobic fluorocarbon domains offer channels for water and CO_2, as confirmed by attenuated total reflectance surface-enhanced infrared absorption spectroscopy (ATR-SEIRAS) and molecule dynamic (MD) simulations. Further analysis reveals that water molecules permeate extensively into the polymer zwitterion channels, forming continuous chains with 1.9 hydrogen bonds per water molecule. Similarly, CO_2 molecules strongly associate with the fluorinated tails of P3, with oxygen atoms facing the ammonium groups. Therefore, the desired amphiphilic interfaces built by the combination of perfluorinated alkanes and hydrophilic phosphorylcholine groups provide a means by which to control mass transport at the complex interface of catalyst-electrolyte-reactant, a promising feature for designing new, efficient catalytic systems for CO_2 electroreduction.

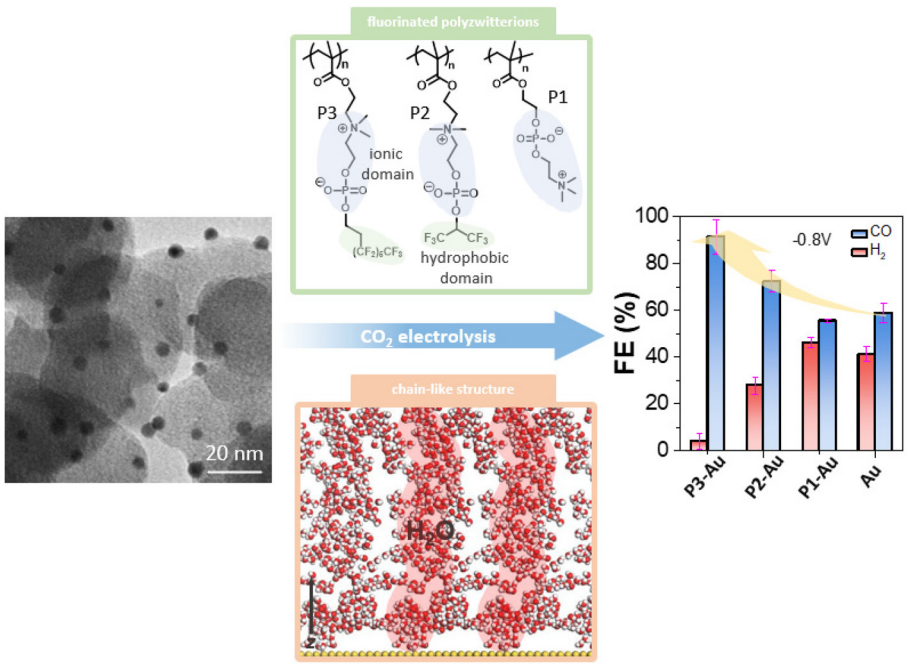

Scheme 1 Scheme illustrating the use of fluorinated polymer zwitterions to control the interfacial microenvironment of AuNPs with enhanced selectivity for CO_2 reduction.

Results and discussion

Polymer zwitterions P1–P3 were prepared by reversible addition–fragmentation chain-transfer (RAFT) polymerization, using methods described previously.[46] P1 and P2 were isolated following their precipitation in diethyl ether, dialysis against deionized water, and lyophilization. P3 was purified by precipitation into a mixture of acetone and diethyl ether, then acetone, and then diethyl ether, followed by drying under vacuum. The number-average molecular weight of polymers was 16.3 kg mol^{-1} for P1 (dispersity $Đ$ 1.1), 21.5 kg mol^{-1} for P2 ($Đ$ 1.25) and 43.9 kg mol^{-1} for P3 ($Đ$ 1.23), respectively (Fig. S1†). AuNPs (an average diameter of 3.2 nm, Scheme 1) were synthesized by direct chemical reduction of HAuCl4 with $NaBH_4$. Before surface modification, AuNPs were first physically adsorbed onto activated carbon (Printex U, ~50 nm nanospheres). The loading ratio of AuNPs on carbon (Au/C) was about 2.5 wt%, also confirmed by scanning electron microscopy with energy dispersive X-ray spectroscopy (SEM-EDX) (see ESI for synthetic details, Fig. S4†). For ligand modification, Au/C catalysts were mixed with polymer zwitterions in trifluoroethanol, which is a good solvent for the polymers. The trithioester chain-ends of P1–P3 serves as a ligand for grafting to AuNP surface.[47] The typical surface modification procedure was carried out over 12 h to promote high surface grafting and the resultant Au/C catalysts were washed thoroughly with centrifugation to remove unbound polymers. The surface modification was confirmed by Fourier-transform infrared spectroscopy (FT-IR) (with pure Au supported on a glass slide see Fig. S2†). After surface grafting, the characteristic vibrational frequency of the polymers with Au/C was compared to that of the free polymers. Taking P1 as an example, the characteristic peaks of P═O at 1229 cm^{-1}, P–O at 1065 cm^{-1}, and P–O–C at 1482 cm^{-1} with quaternary ammonium head-group ($-N^+(CH_3)_3$) at 971 cm^{-1} was seen, indicating successful modification of P1 on the Au nanocatalysts.[48,49] Similarly, typical vibrational peaks of $-CF_2-$ and $-CF_3$ at 1100–1300 cm^{-1} were observed for Au/C catalysts modified with P2 and P3.[50] We used thermogravimetric analysis to analyse the grafting density of polymer zwitterions on AuNPs after surface modification process. The 'grafting to' method showed a 15.7% weight loss for P1, while those were 14.0%, 16.4% for P2 and P3, respectively (Fig. S3†). As a sequence, P1 gave a slightly higher grafting density of 0.76 chains nm^{-2}; while the grafting density was ~0.30 chains nm^{-2} for P2 and P3. Those results are typical for polymer-grafted AuNPs prepared through the grafting-to approach.[51–53]

The electrochemically active surface area (ECSA) of AuNPs was measured by cyclic voltammetry (CV) to assess the impact of polymer zwitterions modification on the accessibility of Au nanocatalysts at electrode–electrolyte interfaces. The CVs were collected in a N_2-saturated 0.5 M H_2SO_4 environment at a scan rate of 100 mV s^{-1} (Fig. 1a). As we can see, during the cathodic scan, a reduction peak appeared at ~1.15 V *vs.* RHE corresponding to the electrochemical reduction of the surface oxygenated monolayer, correlated with the ECSA of AuNPs (Tables S1–S4†). As shown in Fig. 1b, Au/C catalyst in the absence of ligands has an ECSA of 2.8 ± 0.06 cm^2 μg^{-1}. With P1, there is a marginal ECSA change of 2.7 ± 0.03 cm^2 μg^{-1}. Hydrophobic polyzwitterions with fluorinated moieties cause a reduction of surface accessibility of Au. For Au-P2/C and Au-P3/C, the ECSA reduced to 2.1 ± 0.01 and 1.9 ± 0.01 cm^2 μg^{-1}, respectively, attributed to fluorinated moieties blocking contact of ions for electrochemical redox. Linear sweep voltammograms (LSVs) in CO_2-saturated 0.1 M $KHCO_3$ are given in Fig. 1c and d, where the current density was normalized to geometric electrode surface area and ECSA, respectively. In both cases, polymer zwitterions improved the total current density of Au/C as compared to that without ligands. This enhancement was more pronounced when normalized to ECSAs, as evidenced in Fig. 1d.

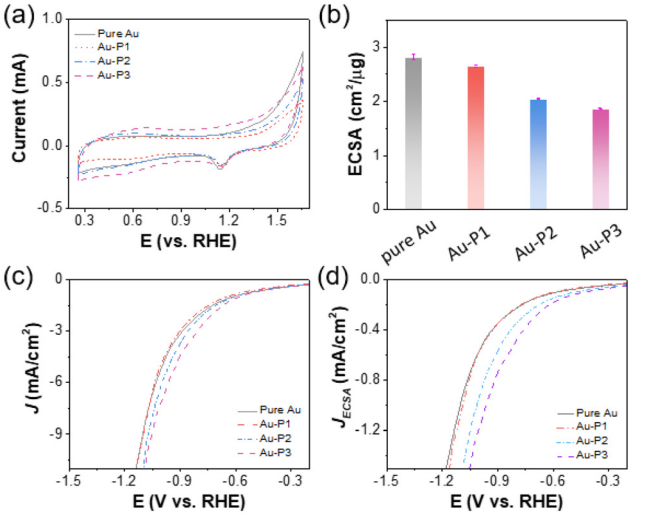

Fig. 1 (a) CV analysis of Au/C modified with fluorinated polymer zwitterions recorded under a scan rate of 100 mV s^{-1} in N_2-saturated 0.5 M H_2SO_4. (b) ECSAs of AuNPs modified with different fluorinated polymer zwitterions. LSV curves measured under a scan rate of 10 mV s^{-1} in CO_2-saturated 0.1 M $KHCO_3$ normalized to (c) geometric area of electrodes and (d) ECSA of AuNPs.

A more quantitative CO_2 electroreduction analysis is presented in Fig. 2. Three parameters, including CO FE, the partial current density (J_{CO} and J_{H_2}), and the product ratio (n_{CO}/n_{H_2}) were employed to compare the electrocatalytic performance of AuNPs with different polyzwitterions as well as citrate-capped Au nanocatalysts as a control. To measure the product of CO_2 electroreduction, a customized H-cell separated using a Nafion membrane was used for all electrocatalytic experiments. In the absence of polyzwitterions, Au/C has low selectivity for CO_2 *vs.* CO, with CO FE ranging of 54%–60% in the potential window of −0.7 to −0.9 V, given their size effects with corner and edge sites favoring HER. Those results agreed well with the literature.[54,55] Fig. 2c plots the potential dependent of partial current density (J_{CO} and J_{H_2}) calculated out from the corresponding FE and overall current density from LSVs. An accelerated kinetics for CO_2 electroreduction was seen under more negative applied bias upon work electrode.

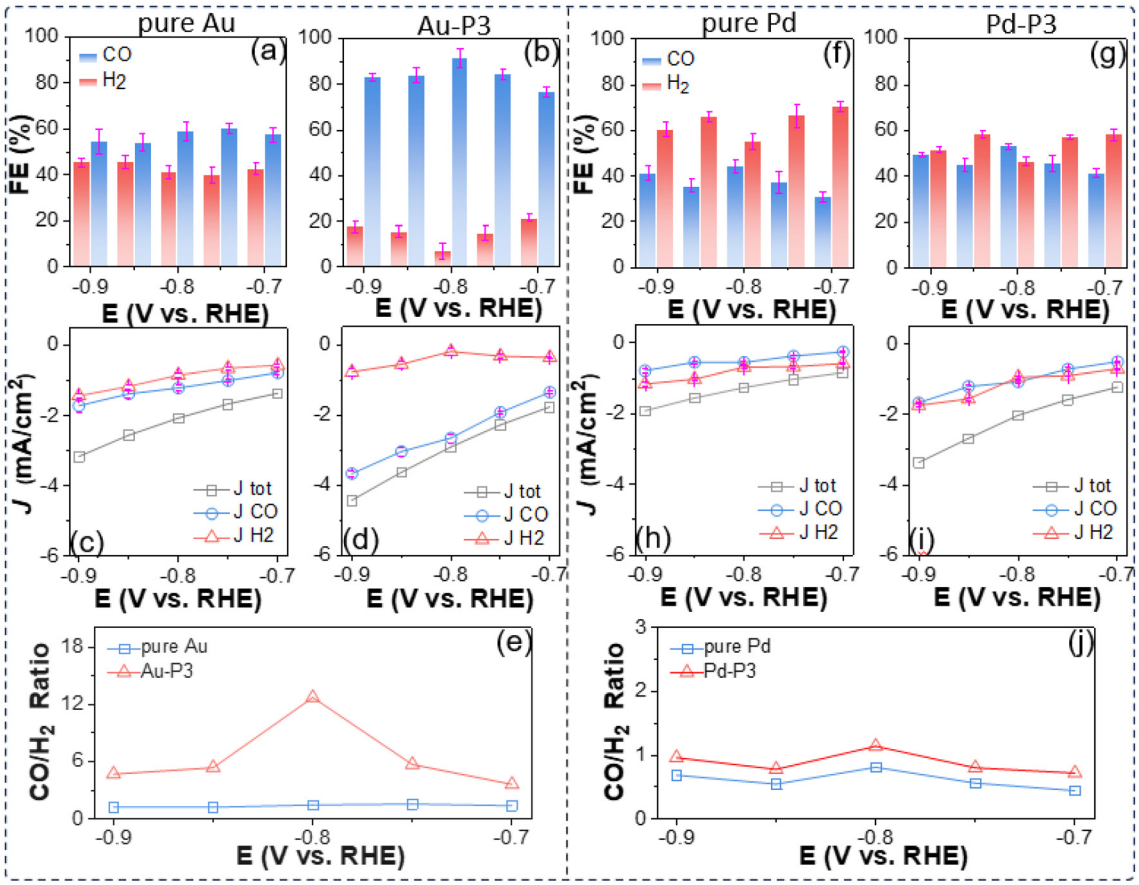

Fig. 2 Electrocatalytic performance for CO_2 reduction: FE and (partial) current density using Au (a and c), Au-P3 (b and d) and the corresponding products ratio (e). FE and (partial) current density using pure Pd (f and h), Pd-P3 (g and i) and the corresponding products ratio (j). A carbon rod was used as a counter electrode and all measurements were carried out in CO_2 saturated 0.1 M $KHCO_3$.

Specifically, J_{CO} reached −1.7 mA cm^{-2} with J_{H_2} of −1.4 mA cm^{-2} at −0.9 V. In the potential window of −0.7 to −0.9 V, unmodified Au/C exhibited a CO to H_2 product ratio around 1.4 (Fig. 2e).

The use of polymer zwitterions resulted in AuNPs exhibiting enhanced selectivity for CO over H_2; in the presence of P3, the CO FE increased to above 80% (Fig. 2b), representing a 20–30% improvement in comparison with unmodified Au/C and a notable enhancement in J_{CO}, outperforming other Au-based nanocatalysts (Table S5†) for CO_2 electroreduction.[54,56–59] For instance, at −0.9 V, Au-P3/C achieved a J_{CO} of 3.7 ± 0.08 mA cm^{-2} (Fig. 2d), approximately 2.6 times higher than that of for Au/C. Fluorinated polymer zwitterions also suppressed the activity to HER. The J_{H_2} values were in the range from 0.21 ± 0.10 to 0.79 ± 0.12 mA cm^{-2} for Au-P3 from −0.7 V to −0.9 V, amounting to approximately 50% decrease to produce hydrogen relative to pure AuNPs. The product ratio of CO/H_2 increased to around 5. At −0.8 V, Au-P3/C exhibited a CO/H_2 ratio of 12.7, as a 9-fold selectivity increase for CO_2 reduction compared to Au/C (Fig. 2e). The embedded fluorinated groups into polyzwitterions are critical for selectivity enhancement. In case of hydrophilic P1, n_{CO}/n_{H_2} dropped to ~1.2, comparable to that of unmodified Au/C (Fig. S5†). In P2, with an hexafluoro isopropyl group, the decrease of fluorocarbon content correlated with a reduction in CO/H_2 ratio to 3.5 at −0.9 V (Fig. S5†). Those results suggest that the presence of the fluorinated domains is essential to create a microenvironment that favors reducing CO_2 over protons. Hydrophilic P1 onto Au/C nanocatalysts had a negligible effect on the overall current density (J_{tot}) or J_{CO}. Adding fluorinated zwitterionic polymers introduced an elevation of J_{CO}, indicating that the amphiphilic interfacial property of fluorinated zwitterionic polymers drives such enhancement.

To validate whether such enhancement resulted from the polyzwitterions, additional control experiments were conducted on a commercially available Pd/C (5 wt% Pd loading). With P3, fluorinated polyzwitterions resulted in an increase of about 10% in the selectivity of Pd/C catalyst to CO_2 reduction within the potential range of −0.7 V to −0.9 V (Fig. 2f and g and Table S6†). Likewise, hydrophobic polyzwitterions enhanced the activity of Pd/C compared to the one without modification (Fig. S6†). Additionally, J_{CO} approached 1.67 ± 0.03 mA cm^{-2} at −0.9 V, around 2.1 times larger than that of Pd/C (Fig. 2h and i). At −0.9 V, commercial Pd/C is more selec-

tive to HER and the FE of CO was 41%; after modification, Pd-P3 had a CO FE of 50%. Similarly, a slightly higher product ratio around 1 for Pd-P3 was observed (Fig. 2j).

In situ ATR-SEIRAS spectroscopy was further used to study how fluorinated polymer zwitterions would change the solid–liquid interface during electrocatalysis. The SEIRAS spectroscopy was conducted on a gold film electrode in the potential range of 0 to −0.9 V with linear scanning voltammetry at a scan rate of 5 mV s^{-1}. Unbiased gold film electrode was used as a background. Any positive absorption peaks (peak up) signify the formation or adsorption of molecular species on the surface, *e.g.*, reaction intermediates during CO_2 electroreduction. Conversely, the downward peaks (peak down) are assigned to desorbed species. Fig. 3a shows the recorded LSV curve in the range of 0 to −0.9 V of pure Au electrode. The corresponding ATR-SEIRAS spectra are presented in Fig. 3b. As cathodic bias increasing, two peaks were seen: a well-defined peak at 1640 cm^{-1}, representing O–H bending (δ_{O-H}) and a broad peak centered at 3300–3600 cm^{-1} for O–H stretching (ν_{O-H}).[60,61] In addition, the peak intensity study was carried out along with the change of applied bias (Fig. 3e). The O–H stretching peak intensity increase rapidly from −0.3 V, indicating the H-down orientation of adsorbed water molecules on the surface of work electrode. The peak centered around 3400 cm^{-1}. With the increase of cathodic bias, the O–H stretching peak had a red-shift forward lower frequency centered at 3350 cm^{-1}, indicating the dynamic process of water absorbed onto the gold surface.[60] At around −0.8 V, the peak intensity plateaued, suggesting the formation of densely packed water molecules on the surface. Those adsorbed water molecules show weak hydrogen bonding as approaching the Au surface.

In the presence of P3, the ATR-SEIRAS spectra displayed noticeable differences. Firstly, the O–H stretching and bending peaks appeared more pronounced under identical potentials (Fig. 3g). The O–H stretching peak also broadened but it centered at 3520 cm^{-1}, suggesting that water molecules did not form extended hydrogen bonding.[62] With applied cathodic

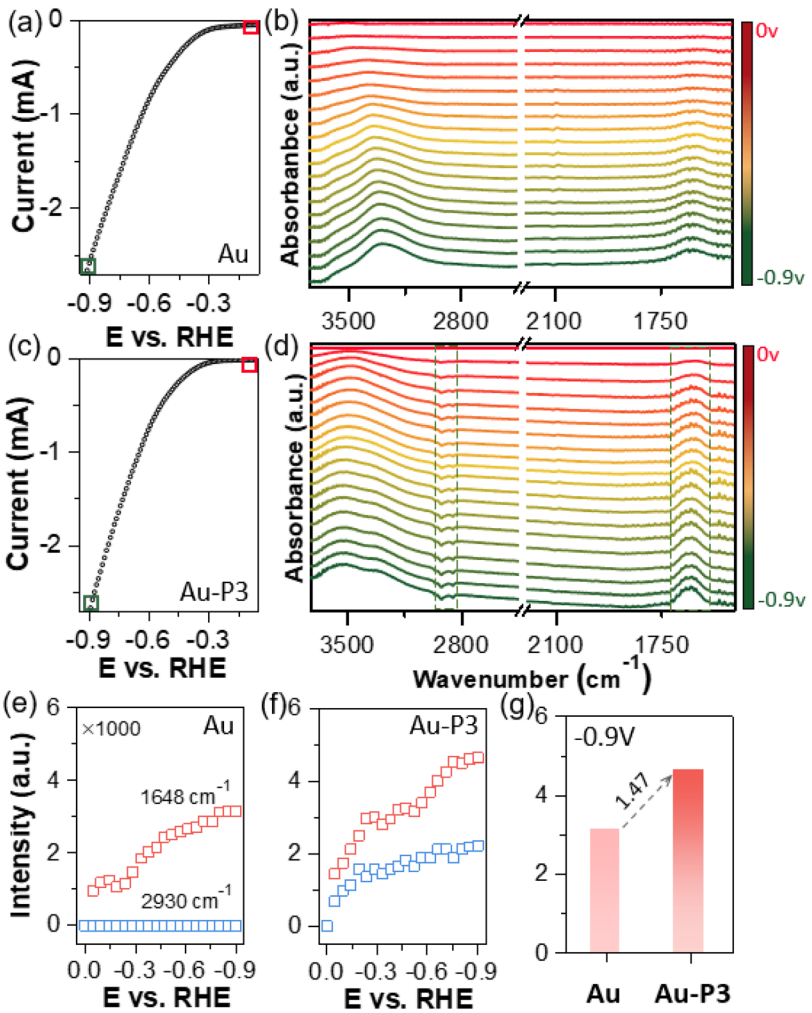

Fig. 3 *In situ* ATR-SEIRAS study of Au electrodes modified with different fluorinated polymer zwitterions. LSV scans in CO_2 saturated 0.1 M $KHCO_3$ and *in situ* ATR-SEIRAS spectra obtained in the range from 0 to −0.9 V for Au (a and b) and Au-P3 (c and d). Peak intensity study for AuNPs (e) and Au-P3 (f) with various reductive potentials. (g) O–H bending model at 1648 cm^{-1} under −0.9 V.

bias, the O–H stretching peak expanded with two shoulders at *ca.* 3520 and 3320 cm^{-1} (Fig. 3c and d). The lower frequency peak nearly overlapped with the O–H stretching peak on pure Au surface, assigned to water molecules with intermolecular hydrogen bonding.[63,64] The new peak appeared at around 3520 cm^{-1} were likely attributed to less hydrogen bonded water. This was also confirmed by Au-P1 and Au-P2. In the presence of polymer zwitterions, a similar O–H stretching peak above 3500 cm^{-1} was observed during electrocatalysis (Fig. S7†). Those water molecules likely reside in zwitterion domains, where choline phosphate groups form strong ion-dipole interaction with water (*i.e.*, hydration). Lastly, with ligands modified Au electrodes as references, the downward peaks at 3000–2800 cm^{-1} were observed along with cathodic applied bias for Au-P3, confirmed from unmodified Au under identical condition with no signals. These peaks are assigned to the C–H stretching of polymer backbones and side chains (see details in Fig. S2†), indicating the decay or the orientation away of modified ligands from the electrode surfaces during electrocatalysis (Fig. 3f).

The wettability of polyzwitterions modified surfaces were examined to investigate the interfacial properties where the electrocatalysis exclusively occurred. As studied by previous literature,[65] fluorocarbon polymers took on appreciable hydrophilicity while small CAs of P1 and P2 are reasonable due to ionic phosphorylcholine. The change of surface hydrophobicity aligned with the electrocatalytic performance of CO_2 reduction, including CO partial current density (J_{CO}) and CO FE. This was confirmed from ligands modification of P1 and P2 with less hydrophobicity showing a lower CO FE and smaller J_{CO} (Fig. S5†), as compared to P3. Furthermore, small-angle X-ray scattering (SAXS) was used to investigate the internal structures of fluorinated polyzwitterions. A distinctive peak at q = 0.21 $Å^{-1}$, corresponding to a D-spacing $\left(D = \frac{2\pi}{q}\right)$ of 3.0 nm, was observed because of the phase separation from hydrophilic and electrostatic interactions of choline phosphate (CP) groups (Fig. S8†). The scattering pattern of P3 can be fitted by a combined cylindrical and lamellar model, indicating the presence of branched cylinders and unstacking lamellae in its fractal morphology. The molecular dynamic (MD) simulation outcome demonstrates the regular separation of P3 with a d-spacing of 2.9 nm (Fig. 4a), consistent with the spacing derived from the corresponding peak in the SAXS data of P3. The phase separation of ionic and fluorinated moieties

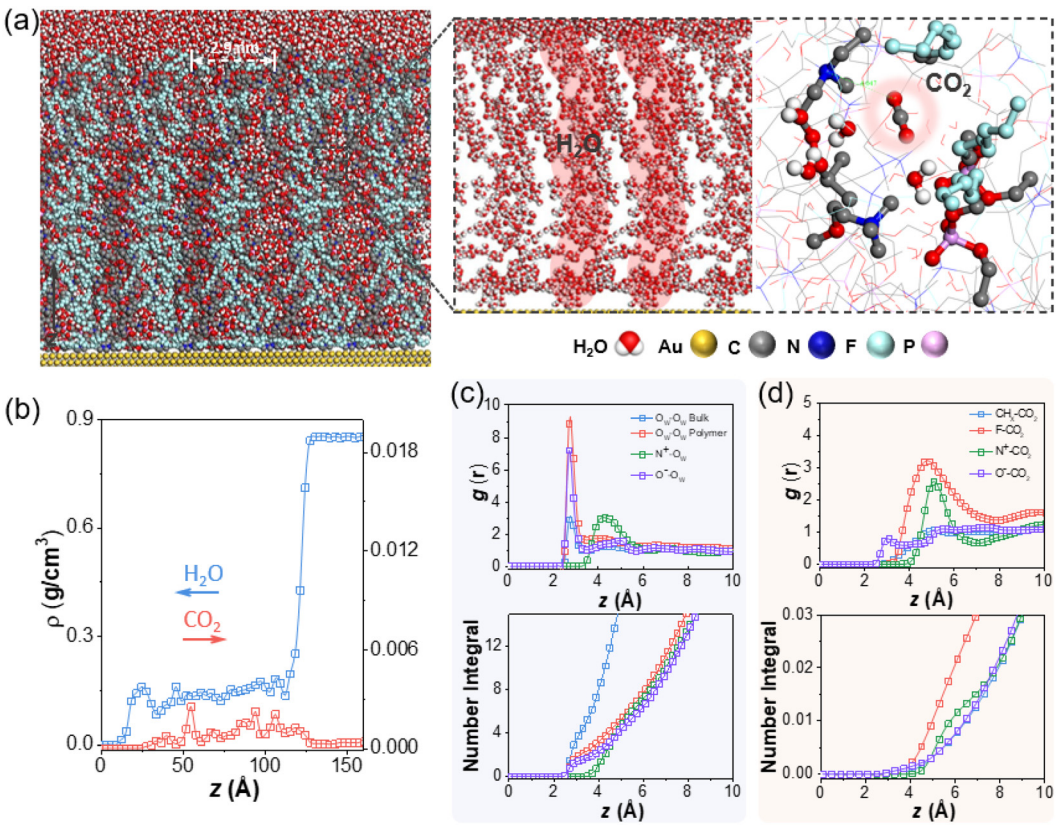

Fig. 4 (a) Snapshot of a representative system configuration (left) and zoomed in area of water distribution and solvated CO_2 molecule (right). (b) Density profiles as a function of z coordinates, with water and CO_2 shown in blue and red. (c) Radial distribution functions and number integrals for O–O of water molecules (O_W–O_W) at z > 12.76 nm (bulk region), O_W–O_W at z < 10.95 nm (polymer layer), N^+–O_W between P3 and water, O^-–O_W between the phosphorous oxygen in P3 and water. (d) Radial distribution functions and number integrals for nonpolar CH_x–CO_2 between polymer backbone and methyl branches and CO_2, CF_x–CO_2 between fluorinated tails of the polymers and CO_2, N^+–CO_2 between P3 and CO_2, O^-–CO_2 between the phosphorous oxygen in P3 and CO_2.

into two domains would have very different affinity to substrates, *e.g.*, proton and CO_2. Together with our SEIRAS results, we would deduce that ionic domains of zwitterions favor the interaction with water, rather than hydrophobic perfluorinated domains.

The effect of zwitterionic ligands on the local solvation environment around AuNPs was investigated using MD simulations. As shown in Fig. 4a, a gold slab was functionalized with P3 ligands at a surface coverage of 0.29 chains per nm^2, with each P3 chain consisting of 50 repeating units and the entire system solvated in water with a bulk water layer thickness of ~ 4.8 nm (Fig. 4b, z > 12.8 nm). Compared to our previous study of AuNPs with hydrophobic polystyrene (Au-PS),[33] the fluorinated zwitterionic P3 similarly resulted in an increased CO_2 concentration in the polymer layer (Fig. 4b). Examining the radial distribution functions (RDFs) for CO_2 (Fig. 4d) and representative snapshots (Fig. 4a), we found that CO_2 molecules most strongly associate with the fluorinated tails of the polymer, with its oxygen atom pointing towards the positively charged amine groups. Similar results are also confirmed with various CO_2 concentrations (Fig. S9†). However, unlike the case of hydrophobic ligands creating pockets of water clusters, water permeates into the P3 polymer layer more extensively to form continuous chains that adsorb preferentially on the zwitterions (Fig. 4c). The number integrals in Fig. 4c show that the first (r < 0.35 nm) and second (0.35 < r < 0.57 nm) solvation shells around phosphate anion contain 1.8 and 4 water molecules, and the loose structure around the ammonium cation atom (r < 0.63 nm) contains 8 water molecules. Similar continuous chains are also confirmed with different CO_2 concentrations (Fig. S10†). To further contrast the water structures induced by the different polymer ligands, we performed a hydrogen-bonding analysis and calculated the tetrahedral order parameter. Here, two water molecules are considered to be connected by a hydrogen bond when r_{OO} < 0.33 nm and ∠O–H···O > 113.58°.[66] Using this criterion, bulk water forms ~3.9 hydrogen bonds per molecule, corresponding to an extended tetrahedral network. By contrast, water molecules in the P3 layer form 1.9 hydrogen bonds by average, consistent with a chain-like structure, while water molecules in polystyrene have 3.1 hydrogen bonds, indicating a more localized cluster-like structure (Fig. S11†). To calculate the tetrahedral order parameter, q, for a water molecule in the polymer layer, its four nearest-neighbor water molecules were considered, regardless of whether they are hydrogen-bonded. The order parameter ranges from −3 to 1 (for a perfect tetrahedron). q reaches 0.6 for bulk water at room temperature, compared to q = 0.20 for the polystyrene ligand, while it is −0.17 in the P3 polymer region, indicating a substantially less ordered 3D structure.

To quantitatively assess how fluorinated polymer zwitterions influence the accessibility of Au related to ions and CO_2, we further measured the interfacial mass transfer kinetics during electrocatalysis using three distinct molecular probes. Fig. 5a and b display the reversible redox CVs of the anionic probe, $K_3Fe(CN)_6$, on Au/C and Au-P3 electrode with scan rates ranging from 80 to 120 mV s^{-1}. A clear linear relationship between peak current (I_p) and the square root of the scan rate (Fig. 5c) enabled examination of the diffusion coefficient of $Fe(CN)_6^{3-}$ using the Randles–Ševčík equation. The diffusion coefficient (D_0) of ferricyanide anions is 1.7 × 10^{-6} cm^2 s^{-1} in the absence of the polymer zwitterions. With polymer zwitterions, the D_0 values exhibited negligible shifts: 1.7 × 10^{-6} cm^2 s^{-1} for Au-P1, 1.4 × 10^{-6} cm^2 s^{-1} for Au-P2, and 1.9 × 10^{-6} cm^2 s^{-1} for Au-P3, respectively (Fig. S12† and Fig. 5d). Polyzwitterions did not slow down the diffusion of ferricyanide anions. Similarly, the

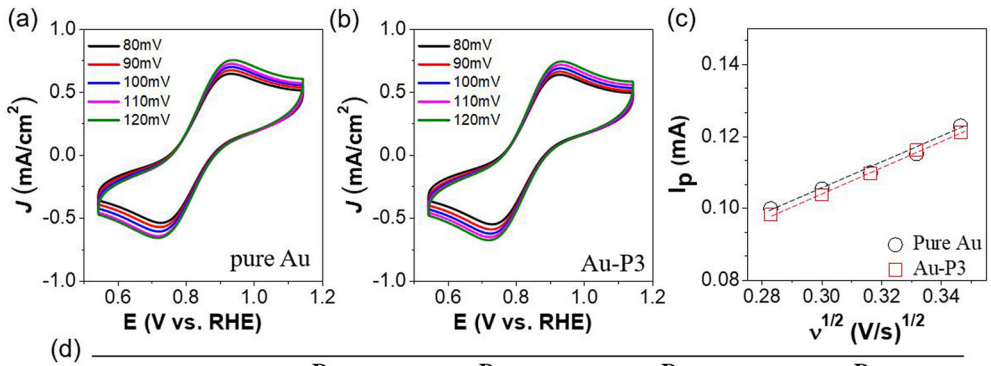

(d)

Sample ID	$D_{Fe(CN)_6^{3-}}$ ($\times10^{-6}$ cm^2 s^{-1})	$D_{Ru(NH_3)_6^{3+}}$ ($\times10^{-5}$ cm^2 s^{-1})	$D_{Fc\text{-}COOH}$ ($\times10^{-6}$ cm^2 s^{-1})	D_{CO_2} ($\times10^{-9}$ cm^2 s^{-1})
Pure Au	1.7±0.09	1.9±0.06	1.6±0.08	0.6
Au-P1	1.7±0.10	1.7±0.09	1.8±0.04	0.7
Au-P2	1.4±0.05	1.8±0.08	2.0±0.09	1.3
Au-P3	1.9±0.03	2.0±0.06	2.5±0.12	2.5

Fig. 5 Mass transport properties of all catalysts. (a) CV scans of AuNPs and (b) Au-P3 measured with 5 mM $K_3Fe(CN)_6$ under various scan rates. (c) Linear relationship between peak current (I_p) and the square root of scan rates for pure Au and Au-P3. (d) Summary of diffusion coefficient (D) using various probe molecules including $Fe(CN)_6^{3-}$, $Ru(NH_3)_6^{3+}$, Fc-COOH, and CO_2.

diffusion coefficient of the cationic probe, $Ru(NH_3)_6^{3+}$, showed a similar trend (Fig. S13†). As $Fe(CN)_6^{3-}$ and $Ru(NH_3)_6^{3+}$ are significantly larger than proton and water, it is reasonable to assume that polyzwitterions would not block the diffusion of protons. The presence of ionic domains in polymer zwitterions would, in some cases, increase the diffusion of ions. For example, for large molecular probes *e.g.*, ferrocene carboxylic acid (Fc-COOH) with slightly more hydrophobicity, the diffusion coefficient increased approximately 20% and 50% in the presence of P2 and P3 (Fig. 5d and Fig. S14†) as compared to pure Au. This enhancement could be attributed to the affinity of the probe for the hydrophobic fluorocarbon-rich domain. To gain insight into the diffusion kinetics of CO_2 during electrocatalysis, electrochemical impedance spectroscopy (EIS) was used to analyze its diffusion at −0.7 V through a frequency range from 100 kHz to 1 Hz (Fig. S15†). The diffusion coefficient of CO_2 approached to 1.3 and 2.5×10^{-9} cm^2 s^{-1} for Au-P2 and Au-P3 with hydrophobic domains, respectively, approximately 2- and 4-fold increase compared to the unmodified Au/C. Even though the EIS measurement could not distinguish CO_2 diffusion from proton contribution, the proton reduction contribution was not less significant for Au catalysts modified by P3.

The diffusion of CO_2 across polymer ligands was also analyzed by MD simulations, revealing the nanosecond time scale, CO_2 motion is sub-diffusive (Fig. S16†) and exhibits a strong anisotropy in the Au-P3 system. If we were to compute an "effective" diffusivity based on the Einstein relationship, the overall diffusion coefficient of CO_2 would be 2×10^{-6} cm^2 s^{-1} while that along the *z*-axis would be 8×10^{-6} cm^2 s^{-1}. This anisotropy was not observed in the Au-polystyrene simulations in which both diffusion coefficients were around 2×10^{-6} cm^2 s^{-1}. Although these effective diffusivities are three orders of magnitude larger than those measured by the EIS experiments, the increase of CO_2 diffusion is dependent on the hydrophobic perfluorinated moieties of P3. We speculate that the difference between experiments and simulation might be due to a combination of two factors. On one hand, the simulations did not account for chemical interactions and interconversion (*e.g.*, carbonate/carbamate formation) between CO_2 and water/zwitterions, which may inhibit CO_2 diffusion. On the other hand, charge transfer reactions of CO_2 may not be fast enough for the EIS measurement to determine true CO_2 diffusivity. Based on the results above, the hydrophobicity from fluorinated subunits likely establishes a localized microenvironment that facilitates transport kinetics and enriches CO_2 near the Au surface.

Conclusions

In summary, this study presents a method for controlling the microenvironment of nanocatalysts by balancing the mass transport of CO_2 and protons during CO_2 electroreduction through fluorinated polyzwitterions. The combination of zwitterions with fluorinated moieties, notably poly(PFO-MCP, P3), provides an effective way to enhance selectivity in CO_2 electroreduction. CO FE increased from *ca.* 60% to 80% for perfluorinated P3 modified AuNPs in the range of −0.7 V to −0.9 V, that is higher than those of small Au nanocatalysts favoring hydrogen product. Furthermore, the partial current density for HER, J_{H_2}, is reduced by approximately 50%. The product ratio analysis indicates that the desired interface improved the CO/H_2 ratio as high as 12.7, 9-fold higher than pure Au. As confirmed by ATR-SEIRAS, MD simulations, SAXS and diffusion estimation, the phase-separated hydrophilic ionic domains and fluorinated domains offered separated channels to regulate reactants, *e.g.*, CO_2 and water. The fluorinated tail acts to adsorb CO_2 molecules; simultaneously, water molecules permeate extensively into the polymer layer on zwitterions, forming continuous chain-like structures with 1.9 hydrogen bonds per molecule in comparison to bulk water with 3.9 hydrogen bonds forming an extended tetrahedral network. Our results highlighted the critical role of localized microenvironments from bioinspired design of surface ligands with enhanced selectivity forward CO_2 reduction.

Author contributions

J. H. and T. E. conceived the concept. Q. L. and M. L. carried out the electrocatalysis experiments, electrochemistry spectroscopic study and analysis. P. B. and J. T. set out the MD simulation process. L. Z. and T. E. designed and synthesized polymer ligands. M-P. N, C-H. L, and H. D. did the SAXS test and analysis. Z. Y. did the surface contact angle analysis. J. H. and Q. L. took the lead in writing the manuscript. All authors here discussed the results and provide suggestions for manuscript.

Data availibility

The data supporting this article have been included as part of the ESI.†

Conflicts of interest

There are no conflicts to declare.

Acknowledgements

JH is grateful for the financial support from the National Science Foundation (CHE 2102245 on CO_2 reduction). PB acknowledges the support from the National Science Foundation (CBET 2144360 on simulation). TE acknowledges support for the synthesis of polymer zwitterions from the Department of Energy, Office of Basic Energy Sciences, Division of Materials Science and Engineering (DE-SC0008876). The TEM images were obtained at the Biosciences Electron Microscopy Facility at the University of Connecticut. This work was also partially supported by the Green

Emulsions Micelles and Surfactants (GEMS) Center of the University of Connecticut. The LiX beamline is part of the Center for BioMolecular Structure (CBMS), which is primarily supported by the National Institutes of Health, National Institute of General Medical Sciences (NIGMS) through a P30 Grant (P30GM133893), and by the DOE Office of Biological and Environmental Research (KP1605010). LiX also received additional support from NIH Grant S10 OD012331. As part of NSLS-II, a national user facility at Brookhaven National Laboratory, work performed at the CBMS is supported in part by the U.S. Department of Energy, Office of Science, Office of Basic Energy Sciences Program under contract number DE-SC0012704. The computer simulations used resources of the National Energy Research Scientific Computing Center (NERSC) through allocation ERCAP0028612 and of the Advanced Cyberinfrastructure Coordination Ecosystem (ACCESS) through allocation CTS190069.

References

1 O. G. Sánchez, Y. Y. Birdja, M. Bulut, J. Vaes, T. Breugelmans and D. Pant, *Curr. Opin. Green Sustain. Chem.*, 2019, **16**, 47–56.
2 Y. Zhang, X. Wang, S. Zheng, B. Yang, Z. Li, J. Lu, Q. Zhang, N. M. Adli, L. Lei, G. Wu and Y. Hou, *Adv. Funct. Mater.*, 2021, **31**, 2104377.
3 B. Chen, B. Li, Z. Tian, W. Liu, W. Liu, W. Sun, K. Wang, L. Chen and J. Jiang, *Adv. Energy Mater.*, 2021, **11**, 2102152.
4 T. Wang, Q. Zhang, K. Lian, G. Qi, Q. Liu, L. Feng, G. Hu, J. Luo and X. Liu, *J. Colloid Interface Sci.*, 2024, **655**, 176–186.
5 A. J. Martín, G. O. Larrazábal and J. Pérez-Ramírez, *Green Chem.*, 2015, **17**, 5114–5130.
6 A. Razmjoo, L. Gakenia Kaigutha, M. A. Vaziri Rad, M. Marzband, A. Davarpanah and M. Denai, *Renewable Energy*, 2021, **164**, 46–57.
7 Z. Yin, G. T. R. Palmore and S. Sun, *Trends Chem.*, 2019, **1**, 739–750.
8 H. Xie, T. Wang, J. Liang, Q. Li and S. Sun, *Nano Today*, 2018, **21**, 41–54.
9 L. Fan, C. Xia, F. Yang, J. Wang, H. Wang and Y. Lu, *Sci. Adv.*, 2020, **6**, eaay3111.
10 R. Shi, J. Guo, X. Zhang, G. I. N. Waterhouse, Z. Han, Y. Zhao, L. Shang, C. Zhou, L. Jiang and T. Zhang, *Nat. Commun.*, 2020, **11**, 3028.
11 D. Wakerley, S. Lamaison, F. Ozanam, N. Menguy, D. Mercier, P. Marcus, M. Fontecave and V. Mougel, *Nat. Mater.*, 2019, **18**, 1222–1227.
12 Y. Chen, R. K. Miao, C. Yu, D. Sinton, K. Xie and E. H. Sargent, *Matter*, 2024, **7**, 25–37.
13 X. Han, T. Mou, S. Liu, M. Ji, Q. Gao, Q. He, H. Xin and H. Zhu, *Nanoscale Horiz.*, 2022, **7**, 508–514.
14 T. Wei, S. Zhang, Q. Liu, Y. Qiu, J. Luo and X. Liu, *Acta Phys.-Chim. Sin.*, 2023, **39**, 202207026.
15 Y. Lin, T. Wang, L. Zhang, G. Zhang, L. Li, Q. Chang, Z. Pang, H. Gao, K. Huang, P. Zhang, Z.-J. Zhao, C. Pei and J. Gong, *Nat. Commun.*, 2023, **14**, 3575.
16 A. S. Varela, *Curr. Opin. Green Sustain. Chem.*, 2020, **26**, 100371.
17 C. Chen, H. Jin, P. Wang, X. Sun, M. Jaroniec, Y. Zheng and S. Z. Qiao, *Chem. Soc. Rev.*, 2024, **53**, 2022–2055.
18 Y. J. Sa, C. W. Lee, S. Y. Lee, J. Na, U. Lee and Y. J. Hwang, *Chem. Soc. Rev.*, 2020, **49**, 6632–6665.
19 Z. Luo, Z. Yin, J. Yu, Y. Yan, B. Hu, R. Nie, A. F. Kolln, X. Wu, R. K. Behera, M. Chen, L. Zhou, F. Liu, B. Wang, W. Huang, S. Zhang and L. Qi, *Small*, 2022, **18**, 2107799.
20 J. Y. T. Kim, C. Sellers, S. Hao, T. P. Senftle and H. Wang, *Nat. Catal.*, 2023, **6**, 1115–1124.
21 D. Raciti, T. Braun, B. M. Tackett, H. Xu, M. Cruz, B. J. Wiley and T. P. Moffat, *ACS Catal.*, 2021, **11**, 11945–11959.
22 X. Zhu, C. Tian, H. Wu, Y. He, L. He, H. Wang, X. Zhuang, H. Liu, C. Xia and S. Dai, *ACS Appl. Mater. Interfaces*, 2018, **10**, 43588–43594.
23 J. Ding, T. Wei, T. Hou, W. Liu, Q. Liu, H. Zhang, J. Luo and X. Liu, *Nanoscale*, 2024, **16**, 10628–10636.
24 A. S. Hall, Y. Yoon, A. Wuttig and Y. Surendranath, *J. Am. Chem. Soc.*, 2015, **137**, 14834–14837.
25 X. Yang, H. Ding, S. Li, S. Zheng, J.-F. Li and F. Pan, *J. Am. Chem. Soc.*, 2024, **146**, 5532–5542.
26 M. R. Singh, Y. Kwon, Y. Lum, J. W. Ager III and A. T. Bell, *J. Am. Chem. Soc.*, 2016, **138**, 13006–13012.
27 Q. Zhu, C. J. Murphy and L. R. Baker, *J. Am. Chem. Soc.*, 2022, **144**, 2829–2840.
28 F. P. García de Arquer, C.-T. Dinh, A. Ozden, J. Wicks, C. McCallum, A. R. Kirmani, D.-H. Nam, C. Gabardo, A. Seifitokaldani, X. Wang, Y. C. Li, F. Li, J. Edwards, L. J. Richter, S. J. Thorpe, D. Sinton and E. H. Sargent, *Science*, 2020, **367**, 661–666.
29 J. J. Lv, R. Yin, L. Zhou, J. Li, R. Kikas, T. Xu, Z. J. Wang, H. Jin, X. Wang and S. Wang, *Angew. Chem., Int. Ed.*, 2022, **61**, e202207252.
30 A. K. Buckley, M. Lee, T. Cheng, R. V. Kazantsev, D. M. Larson, W. A. Goddard III, F. D. Toste and F. M. Toma, *J. Am. Chem. Soc.*, 2019, **141**, 7355–7364.
31 X. Wei, G. Johnson, Y. Ye, M. Cui, S.-W. Yu, Y. Ran, J. Cai, Z. Liu, X. Chen, W. Gao, P. J. L. Bean, W. Zhang, T. Y. Zhao, F. A. Perras, E. J. Crumlin, X. Zhang, R. J. Davis, Z. Wu and S. Zhang, *J. Am. Chem. Soc.*, 2023, **145**, 14298–14306.
32 K. M. Koczkur, S. Mourdikoudis, L. Polavarapu and S. E. Skrabalak, *Dalton Trans.*, 2015, **44**, 17883–17905.
33 Q. Luo, H. Duan, M. C. McLaughlin, K. Wei, J. Tapia, J. A. Adewuyi, S. Shuster, M. Liaqat, S. L. Suib, G. Ung, P. Bai, S. Sun and J. He, *Chem. Sci.*, 2023, **14**, 9664–9677.
34 L. Zhang, Z. Wei, S. Thanneeru, M. Meng, M. Kruzyk, G. Ung, B. Liu and J. He, *Angew. Chem., Int. Ed.*, 2019, **58**, 15834–15840.
35 S. Zhang, P. Kang, S. Ubnoske, M. K. Brennaman, N. Song, R. L. House, J. T. Glass and T. J. Meyer, *J. Am. Chem. Soc.*, 2014, **136**, 7845–7848.
36 K. Shi, Z. Ren, Z. Meng and X. Feng, *ChemCatChem*, 2023, e202301308.
37 X. Han, Q. Gao, Z. Yan, M. Ji, C. Long and H. Zhu, *Nanoscale*, 2021, **13**, 1515–1528.

38 Z. Wei, C.-H. Liu, Q. Luo, S. Thanneeru, A. M. Angeles-Boza, M.-P. Nieh and J. He, *Mater. Chem. Front.*, 2023, **7**, 2038–2048.
39 Z. Wei and J. He, in *Hairy Nanoparticles*, 2023, pp. 375–400, DOI: **10.1002/9783527835874.ch10**.
40 Y. Zhao, C. Wang, Y. Liu, D. R. MacFarlane and G. G. Wallace, *Adv. Energy Mater.*, 2018, **8**, 1801400.
41 D. Kim, S. Yu, F. Zheng, I. Roh, Y. Li, S. Louisia, Z. Qi, G. A. Somorjai, H. Frei, L.-W. Wang and P. Yang, *Nat. Energy*, 2020, **5**, 1032–1042.
42 Y. Ma, J. Wang, J. Yu, J. Zhou, X. Zhou, H. Li, Z. He, H. Long, Y. Wang, P. Lu, J. Yin, H. Sun, Z. Zhang and Z. Fan, *Matter*, 2021, **4**, 888–926.
43 Q. Chang, J. H. Lee, Y. Liu, Z. Xie, S. Hwang, N. S. Marinkovic, A. A. Park, S. Kattel and J. G. Chen, *JACS Au*, 2022, **2**, 214–222.
44 J. Bai, W. Wang and J. Liu, *Chemistry*, 2023, **29**, e202302461.
45 K. Wei, H. Guan, Q. Luo, J. He and S. Sun, *Nanoscale*, 2022, **14**, 11869–11891.
46 L. Zhou, A. Triozzi, M. Figueiredo and T. Emrick, *ACS Macro Lett.*, 2021, **10**, 1204–1209.
47 B. Ebeling and P. Vana, *Macromolecules*, 2013, **46**, 4862–4871.
48 L. Jiang, W. Zhu, H. Qian, C. Wang, Y. Chen and P. Liu, *J. Mater. Chem. B*, 2019, **7**, 5078–5088.
49 L. Zhu, Q. Jin, J. Xu, J. Ji and J. Shen, *J. Appl. Polym. Sci.*, 2009, **113**, 351–357.
50 I. C. P. Rodrigues, L. F. Woigt, K. D. Pereira, A. D. Luchessi, É. S. N. Lopes, T. J. Webster and L. P. Gabriel, *J. Mater. Res. Technol.*, 2020, **9**, 7777–7785.
51 H. Duan, Y. Lin and J. He, in *World Scientific Reference on Plasmonic Nanomaterials*, World Scientific, 2021, vol. 22, pp. 409–432.
52 Z. Wei, M. Kayceety, A. Price, K. Wei, Q. Luo, S. Thanneeru, S. Sun and J. He, *ACS Appl. Mater. Interfaces*, 2022, **14**, 55227–55237.
53 L. Zhang, Z. Wei, M. Meng, G. Ung and J. He, *J. Mater. Chem. A*, 2020, **8**, 15900–15908.
54 W. Zhu, R. Michalsky, Ö. Metin, H. Lv, S. Guo, C. J. Wright, X. Sun, A. A. Peterson and S. Sun, *J. Am. Chem. Soc.*, 2013, **135**, 16833–16836.
55 D.-R. Yang, L. Liu, Q. Zhang, Y. Shi, Y. Zhou, C. Liu, F.-B. Wang and X.-H. Xia, *Sci. Bull.*, 2020, **65**, 796–802.
56 W. Zhu, Y.-J. Zhang, H. Zhang, H. Lv, Q. Li, R. Michalsky, A. A. Peterson and S. Sun, *J. Am. Chem. Soc.*, 2014, **136**, 16132–16135.
57 Z.-H. Gao, K. Wei, T. Wu, J. Dong, D.-e. Jiang, S. Sun and L.-S. Wang, *J. Am. Chem. Soc.*, 2022, **144**, 5258–5262.
58 D. R. Kauffman, D. Alfonso, C. Matranga, H. Qian and R. Jin, *J. Am. Chem. Soc.*, 2012, **134**, 10237–10243.
59 X. Cai, G. Li, W. Hu and Y. Zhu, *ACS Catal.*, 2022, **12**, 10638–10653.
60 M. Dunwell, Y. Yan and B. Xu, *Surf. Sci.*, 2016, **650**, 51–56.
61 S. Zhu, T. Li, W.-B. Cai and M. Shao, *ACS Energy Lett.*, 2019, **4**, 682–689.
62 H. Wang, J. C. Wagner, W. Chen, C. Wang and W. Xiong, *Proc. Natl. Acad. Sci. U. S. A.*, 2020, **117**, 23385–23392.
63 K. Kong, A.-Z. Li, Y. Wang, Q. Shi, J. Li, K. Ji and H. Duan, *Nat. Commun.*, 2023, **14**, 6925.
64 Y.-H. Wang, S. Zheng, W.-M. Yang, R.-Y. Zhou, Q.-F. He, P. Radjenovic, J.-C. Dong, S. Li, J. Zheng, Z.-L. Yang, G. Attard, F. Pan, Z.-Q. Tian and J.-F. Li, *Nature*, 2021, **600**, 81–85.
65 L. Zhou, Z. Yang, J. N. Pagaduan and T. Emrick, *Polym. Chem.*, 2023, **14**, 32–36.
66 J. R. Errington and P. G. Debenedetti, *Nature*, 2001, **409**, 318–321.